

Anomalous parallel momentum transport due to $E \times B$ flow shear in a tokamak plasma

Cite as: Phys. Plasmas **16**, 092303 (2009); <https://doi.org/10.1063/1.3227650>

Submitted: 16 July 2009 • Accepted: 24 August 2009 • Published Online: 15 September 2009

F. J. Casson, A. G. Peeters, Y. Camenen, et al.



View Online



Export Citation

ARTICLES YOU MAY BE INTERESTED IN

[Comparisons and physics basis of tokamak transport models and turbulence simulations](#)

Physics of Plasmas **7**, 969 (2000); <https://doi.org/10.1063/1.873896>

[Linear gyrokinetic calculations of toroidal momentum transport in a tokamak due to the ion temperature gradient mode](#)

Physics of Plasmas **12**, 072515 (2005); <https://doi.org/10.1063/1.1949608>

[Effects of \$E \times B\$ velocity shear and magnetic shear on turbulence and transport in magnetic confinement devices](#)

Physics of Plasmas **4**, 1499 (1997); <https://doi.org/10.1063/1.872367>



Physics of Plasmas Physics of Fluids
Special Topic: Turbulence in Plasmas and Fluids
Submit Today!

Anomalous parallel momentum transport due to $E \times B$ flow shear in a tokamak plasma

F. J. Casson,¹ A. G. Peeters,¹ Y. Camenen,¹ W. A. Hornsby,¹ A. P. Snodin,¹ D. Strintzi,² and G. Szepesi¹

¹Centre for Fusion, Space and Astrophysics, University of Warwick, CV4 7AL Coventry, United Kingdom

²National Technical University of Athens, GR-157 73 Athens, Greece

(Received 16 July 2009; accepted 24 August 2009; published online 15 September 2009)

Nondiffusive anomalous momentum transport in toroidal plasmas occurs through symmetry breaking mechanisms. In this paper the contribution of sheared $E \times B$ flows to parallel momentum transport [R. R. Dominguez and G. M. Staebler, *Phys Fluids B* **5**, 3876 (1993)] is investigated with nonlinear gyrokinetic simulations in toroidal geometry. The background perpendicular shear is treated independently from the parallel velocity shear to isolate a nondiffusive, nonpinch contribution to the parallel momentum flux. It is found that the size of the term depends strongly on the magnetic shear, with the sign reversing for negative magnetic shear. Perpendicular shear flows are responsible for both symmetry breaking and suppression of turbulence, resulting in a shearing rate at which there is a maximum contribution to the momentum transport. The $E \times B$ momentum transport is shown to be quenched by increasing flow shear more strongly than the standard linear quench rule for turbulent heat diffusivity. © 2009 American Institute of Physics. [doi:10.1063/1.3227650]

I. INTRODUCTION

A growing body of experimental evidence^{1–11} now demonstrates that tokamak plasmas can exhibit toroidal rotation even in the absence of an external torque. This “spontaneous” (or “intrinsic”) rotation has generated much recent theoretical attention in mechanisms of anomalous momentum transport beyond the diffusional paradigm.^{12–32} Plasma rotation is of practical importance since it is widely accepted that sheared flows play a role in regulating microturbulent transport,^{33,34} and are associated with the formation of transport barriers.^{35,36} The theory of toroidal momentum transport is not yet complete, but it is clear that a comprehensive description will contain a number of the components that are currently emerging.

In Ref. 15, it was shown from the symmetry of the local gyrokinetic equation that for axisymmetric nonrotating plasmas with up-down flux surface symmetry, there can be no net radial transport of parallel momentum. By breaking the symmetry assumptions of the derivation,¹⁵ nondiffusive contributions to the momentum transport can be present. These contributions, which do not fit well into the transport matrix picture, each arise due to a symmetry breaking mechanism, which can also be viewed in the framework of wave-particle momentum exchange.²⁵ A number of symmetry breaking mechanisms leading to parallel momentum transport have so far been identified:

- In a plasma with an initial rotation, parallel velocity symmetry is broken by the Coriolis drift. The resulting phase difference between density and velocity fluctuations generates a “pinch” transport of parallel momentum, which can sustain finite rotation gradients in a source free region.^{18–21}

- Recently, flux surface shaping asymmetric about the horizontal axis (typical in single null plasmas) has also been shown to generate net momentum transport, providing a “seed” rotation mechanism to build an initial rotation gradient in the outer core.^{27,28}
- In a global model, terms of order ρ_* contribute off diagonal terms to the transport matrix, resulting in a coupling of the heat, momentum, and particle transport channels, as has been evidenced in global gyrokinetic simulations.¹⁷
- A nondiffusive, nonpinch contribution to parallel momentum transport due to sheared background $E \times B$ flow was first identified in a sheared slab quasilinear model in Ref. 12, in which the anomalous parallel stress was found to be nonzero through numerical solution of the system.

The focus of the present work is on the last of the above mechanisms; the contribution of sheared $E \times B$ flow to momentum transport. We reserve pinch to refer to a transport term proportional to the quantity that is being transported; under this definition we do not refer to the $E \times B$ shear term as a pinch.

The turbulent flux of parallel momentum is calculated from the perturbed distribution f as

$$\Gamma_{\parallel} = m_i \left\langle 2\pi B \int \nabla r \cdot \tilde{\mathbf{v}}_E v_{\parallel} dv_{\parallel} d\mu \right\rangle, \quad (1)$$

where the angle brackets denote the flux surface average and $\tilde{\mathbf{v}}_E$ are the $E \times B$ drifts arising from the perturbed electric field. Motivated by the linear theory of the Coriolis pinch¹⁸ and geometric symmetry breaking,²⁷ we write the parallel momentum flux in the local limit as the sum of four components

$$\Gamma_{\parallel} = n_i m_i (\chi_{\parallel} u'_{\parallel} + V_{\phi} u_{\parallel} + \gamma_E M_{\parallel} + C_{\parallel}), \quad (2)$$

where n_i is ion number density and m_i is the ion mass. The first term is the diffusive term due to the gradient in the parallel flow $u'_{\parallel} = -(B_i/B) R \nabla \Omega$, where Ω is the plasma cofield rotation frequency, the second term is the Coriolis pinch dependent on the parallel flow¹⁸ $u_{\parallel} = (B_i/B) R \Omega$, the third term is due to the background $\mathbf{E} \times \mathbf{B}$ shear,¹² and the final term is due to the up-down flux surface asymmetry.²⁷ In the linear models of Refs. 18 and 27, it is assumed that the fluctuation amplitudes in temperature, density, and potential scale together, such that the dimensionless ratios V_{ϕ}/χ_i , χ_{\parallel}/χ_i , and C_{\parallel}/χ_i are roughly constant (with χ_i the ion heat diffusivity). We use the decomposition of Eq. (2) as a heuristic framework in which to examine the $\mathbf{E} \times \mathbf{B}$ contribution to momentum transport. This work makes clear, however, that the linear models which motivate this picture do not easily extend to the nonlinear regime with $\gamma_E \neq 0$. The transport ratio scalings based on fluctuation amplitudes neglect the cross-phase dependence of the fluctuations, which is calculated for the slab in the quasilinear weights of Ref. 12, and retained in the present work through fully nonlinear simulations in toroidal geometry. We stress that in this work M_{\parallel} represents the $\mathbf{E} \times \mathbf{B}$ contribution to parallel momentum transport, not the Mach number.

We define the $\mathbf{E} \times \mathbf{B}$ shearing rate γ_E as a flux function

$$\gamma_E = \frac{1}{B_0} \frac{\partial^2 \Phi}{\partial r^2}, \quad (3)$$

where Φ is the background electric potential, $r = (R_{\max} - R_{\min})/2$ and B_0 is the magnetic field evaluated on the magnetic axis.³⁷ The background $\mathbf{E} \times \mathbf{B}$ flow is defined to be zero in the center of the local radial domain simulated.

In a conventional large aspect ratio tokamak, the toroidal component of the parallel momentum dominates, and neo-classical mechanisms damp the poloidal flows. For the present work it is assumed then that transport of parallel momentum is approximately equivalent to the transport of toroidal angular momentum ($\Gamma_{\parallel} \approx \Gamma_{\phi}$).

A sheared toroidal rotation has a parallel shear component u'_{\parallel} , which is coupled to a perpendicular shear component γ_E . Sheared $\mathbf{E} \times \mathbf{B}$ flow can also be present independent of u'_{\parallel} , as the perpendicular component of a sheared poloidal flow (either neoclassically given by $v_{\theta} = (k_{\text{neo}}/eB) dT/dr$ or anomalous). Global fluid simulations of internal transport barriers (ITBs) have included the $\mathbf{E} \times \mathbf{B}$ contribution to momentum transport with a quasilinear model, keeping both parts of the $\mathbf{E} \times \mathbf{B}$ shear consistently with global temperature and rotation profiles.¹³ Later, a cylindrical fluid model²³ also used a quasilinear model for the parallel stress to elucidate the parallel symmetry breaking mechanism leading to momentum transport. Local gyrokinetic simulations with sheared toroidal rotation^{16,22} have indicated a sizeable correction to the momentum diffusivity, also seen in recent global gyrokinetic particle-in-cell simulations.^{31,32} In Ref. 22, parallel and perpendicular flow shears were varied independently (i.e., not pure toroidal rotation) to identify null flow points.

In the present work, we investigate the effect of sheared perpendicular flow (γ_E) on momentum transport, independently from sheared parallel flow (u'_{\parallel}). We also examine the case of purely toroidal rotation, motivated by experimental observations of $v_{\theta} \ll v_{\phi}$ (e.g., Ref. 7). Local nonlinear gyrokinetic simulations with $\mathbf{E} \times \mathbf{B}$ shear performed with the GKW code^{14,37} are presented, and the resulting momentum transport is shown to exhibit a strong dependence on the magnetic shear and direction of the plasma current.

This paper is structured as follows: Section II introduces the basic parameters of the simulated system; Sec. III describes a benchmark of the background $\mathbf{E} \times \mathbf{B}$ shear, Sec. IV presents the results for parallel momentum transport, and conclusions are drawn in Sec. V.

II. SYSTEM DESCRIPTION, UNITS, AND CONVENTIONS

Nonlinear electrostatic gyrokinetic simulations in toroidal geometry are performed with the Vlasov flux tube code GKW.^{14,37} A full description of the code is detailed in Ref. 37 and the code is available from the associated library. All simulations were performed for the collisionless Waltz standard case^{34,38,39} of a deuterium plasma with $R/L_T = 9$, $R/L_N = 3$, electron to ion temperature ratio $T_e/T_i = 1$, mass ratio $\sqrt{m_i/m_e} = 60$, safety factor $q = 2$, magnetic shear $\hat{s} = 1$, and inverse aspect ratio $\epsilon = r/R = 0.16$ unless stated otherwise. The geometry used is the “ $s-\alpha$ ” model, which assumes circular flux surfaces with the magnetohydrodynamic parameter $\alpha = 0$, with geometry quantities evaluated to only lowest order in ϵ .

The sign of the momentum flux will depend on a number of other quantities, so for clarity and convenience we define

$$\begin{aligned} s_B &= \text{sign}(\mathbf{B} \cdot \nabla \phi) = \pm 1, \\ s_j &= \text{sign}(\mathbf{j} \cdot \nabla \phi) = \pm 1, \\ s_{\hat{s}} &= \text{sign}(\hat{s}) = \pm 1, \\ s_{\gamma} &= \text{sign}(\gamma_E) = -\text{sign}(\nabla E_r \cdot \nabla r) = \pm 1, \end{aligned} \quad (4)$$

where ϕ is the toroidal angle clockwise viewed from above. Unless otherwise stated, all simulations were performed with $s_B = s_j = s_{\gamma} = 1$. We define q as always positive, since s_j determines the direction of the poloidal field. In the case of a purely toroidal rotation, the poloidal components of the parallel flow and the $\mathbf{E} \times \mathbf{B}$ flow cancel to give $\gamma_E = s_B s_j (\epsilon/q) u'_{\parallel}$ (with q always positive). We define $u_{\parallel} > 0$ as flow in the direction of \mathbf{B} , with the result that a peaked toroidal flow profile (in the direction of \mathbf{B}) has $s_{\gamma} s_B s_j = 1$.

Results are presented in the standard gyro-Bohm units where a is the plasma minor radius, $c_s = \sqrt{T_e/m_i}$ is the ion sound speed, $\rho_s = c_s/\Omega_{ci}$ is the ion-sound Larmor radius, and $\Omega_{ci} = eB/m_i$ is the ion cyclotron frequency evaluated on the magnetic axis. Unless otherwise stated, all simulations with adiabatic electrons are performed with $N_{\text{mod}} = 16$ binormal modes and $N_x = 83$ radial modes. The maximum wave vector has binormal wave number $k_{\perp} \rho_s = 0.75$, where k_{\perp} is evaluated at the outboard midplane and ρ_s is evaluated at the mag-

TABLE I. Most unstable linear modes: Growth rate γ_{\max} , with corresponding mode frequency ω and scale $k_{\perp}\rho_s$. Positive values of ω indicate propagation in the ion diamagnetic direction.

\hat{s}	$\gamma_{\max}(a/c_s)$	$\omega(a/c_s)$	$k_{\perp}\rho_s$
Adiabatic electrons			
-0.50	0.119	0.272	0.44
-0.17	0.144	0.278	0.44
0.00	0.159	0.286	0.44
0.17	0.175	0.303	0.44
0.34	0.186	0.313	0.43
0.50	0.190	0.329	0.40
0.68	0.178	0.330	0.38
1.00	0.132	0.296	0.31
Kinetic electrons			
1.00	0.265	0.324	0.28

netic axis. The mode spacing gives a perpendicular simulation domain of extent $[L_{\text{radial}}, L_{\text{binormal}}] = [120, 126]\rho_s$. The number of grid points in parallel velocity, magnetic moment, and along the field line are $N_{v\parallel} = 16$, $N_{\mu} = 8$, and $N_s = 16$, respectively. These grid sizes have proved sufficient to investigate the physics phenomena. The results are fully converged in N_s , N_{μ} , and N_x , and to within 20% in N_{mod} and $N_{v\parallel}$. All simulations with kinetic electrons are performed with $N_{\text{mod}} = 21$ binormal modes with a maximum $k_{\perp}\rho_s = 1.0$ and $N_x = 167$ radial modes with a perpendicular simulation domain of extent $[L_{\text{radial}}, L_{\text{binormal}}] = [120, 126]\rho_s$. The number of points in the parallel velocity is increased to $N_{v\parallel} = 32$ as compared with the adiabatic case. Unless otherwise stated, results presented are for adiabatic electrons.

Previous work⁴⁰ has found that shear flow quenching of heat transport follows the phenomenological relation for the turbulent diffusivity

$$\chi_i = \chi_{i0}(1 - \alpha_E \gamma_E / \gamma_{\max}), \quad (5)$$

where α_E is a constant of order unity, and γ_{\max} is the maximum linear growth rate of the system in the absence of the sheared flow. The values of γ_{\max} and other linear properties for the simulations in this paper are given in Table I and most results are presented in terms of γ_E / γ_{\max} . The spectrum of linear growth rates is shown in Fig. 1.

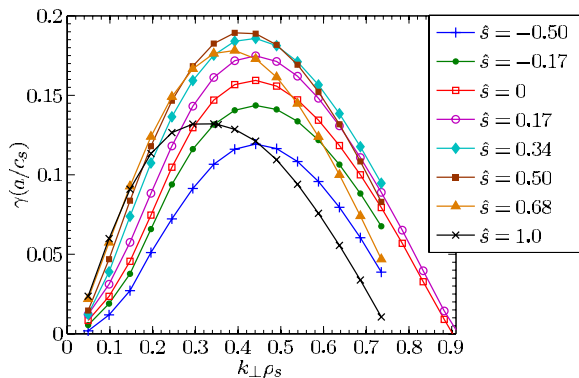


FIG. 1. (Color online) Adiabatic ITG growth rate spectra for different values of \hat{s} . For values of $\hat{s} > 0.5$, the spectrum peaks at lower $k_{\perp}\rho_s$.

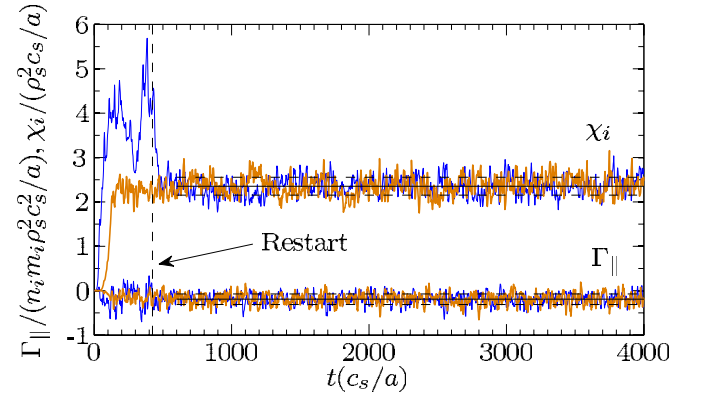


FIG. 2. (Color online) Time traces of ion heat diffusivity and momentum flux for the restart method (blue, thin) compared to a run without restart (orange, thick) with $\gamma_E = 0.118(c_s/a)$ with means and variances $\bar{\chi}_i = (2.354 \pm 0.202, 2.353 \pm 0.218)$ and $\bar{\Gamma}_{\parallel} = (-0.191 \pm 0.119, -0.188 \pm 0.127)$ for the restart and nonrestart methods, respectively.

In simulations with a high $\mathbf{E} \times \mathbf{B}$ shear rate, the linear growth is suppressed such that the simulation takes an impractically long time to reach the nonlinear saturated state. However, if the simulation is initialized without background $\mathbf{E} \times \mathbf{B}$ shear, and the shear is applied once the nonlinear phase is reached, then the system will quickly reach a new saturated state. We find that the statistical properties of the saturated nonlinear state are unaffected by the path taken to get there (Fig. 2), and all results presented here were obtained with the restart method for larger γ_E . All time averages were taken over a minimum range of $t_{\text{av}} = 1600(a/c_s)$ after the new saturated state was reached, unless otherwise specified.

III. NONLINEAR BACKGROUND $\mathbf{E} \times \mathbf{B}$ SHEAR BENCHMARK

The GKW implementation of the background $\mathbf{E} \times \mathbf{B}$ shear³⁷ was benchmarked against previous results¹⁶ from the GYRO code⁴¹ for the Waltz standard case, for both kinetic and adiabatic electrons. Both codes were run in the local limit with the model $s-\alpha$ equilibrium in which the shearing rate for both codes is equivalent to the familiar definition:^{42,43}

$$\gamma_E \approx \frac{(RB_p)^2}{B_t} \frac{\partial^2 \Phi}{\partial \Psi^2} \approx \frac{dv_E}{dr}, \quad (6)$$

where Ψ is the poloidal flux.

The GKW simulations were run with the resolution described above, which are comparable to the grid sizes used in Ref. 16 (although it should be noted that the numerics of the codes are different). In particular, both sets of results were obtained with $N_{\text{mod}} = 16$ binormal modes over the same range of wave numbers.

In GKW the $\mathbf{E} \times \mathbf{B}$ shear is implemented with a discrete wave vector remapping method,^{37,44} for which convergence in radial resolution $L_{\text{radial}}/L_{\text{binormal}}$ should be checked; Fig. 3 demonstrates the results are well converged in this sense. The variance of the fluxes in the nonlinear phase decreases with increasing L_{radial} (since the average is over a larger radial domain) but the mean is converged to within 5%. For

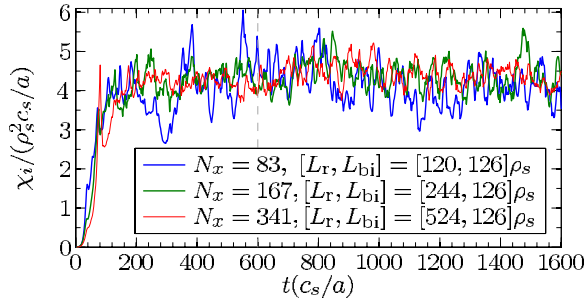


FIG. 3. (Color online) $L_{\text{radial}}/L_{\text{binormal}}$ convergence check of the $\mathbf{E} \times \mathbf{B}$ shearing implemented in GWK, with L_{binormal} held constant. The test is most important for small values of γ_E ; here $\gamma_E = 0.024(c_s/a)$. The values of the averages over $t_{\text{av}} = 1000(a/c_s)$ are $\bar{\chi}_i^{120}(a/c_s \rho_s^2) = 4.16 \pm 0.50$, $\bar{\chi}_i^{244}(a/c_s \rho_s^2) = 4.38 \pm 0.38$, and $\bar{\chi}_i^{524}(a/c_s \rho_s^2) = 4.42 \pm 0.29$, with increasing L_{radial} .

these results, the shear was applied from $t=0$.

The correspondence between the linear growth rates predicted by GWK (Table I) and GYRO (Table I of Ref. 16) is nearly exact. The comparison between the two codes for the nonlinear turbulent ion diffusivity quenching with shearing is shown in Fig. 4 and the GWK results are summarized in Table II. It can be seen that GWK diffusivities are up to 25% higher, which may be due to a difference between the codes in the treatment of the radial boundary condition. It is likely, however, that closer agreement could be obtained in a benchmark undertaken collaboratively with full convergence as the aim.

Notwithstanding the above, GWK and GYRO give good agreement for the turbulence quench relation [Eq. (5)] with close concurrence on the important parameter $\alpha_E \approx 0.4-0.6$ (depending on the case), which quantifies the strength of the shear suppression. This agreement gives good confidence in the qualitative physics predicted by both codes.

For adiabatic electrons, the benchmark was also conducted including the destabilizing effect of parallel velocity shear $u_{\parallel}' = 12\gamma_E$ consistently for purely toroidal rotation, also shown in Fig. 4. Here too the codes give good agreement, both predicting a minimum in the heat transport at $\gamma_E = 2\gamma_{\text{max}}$.

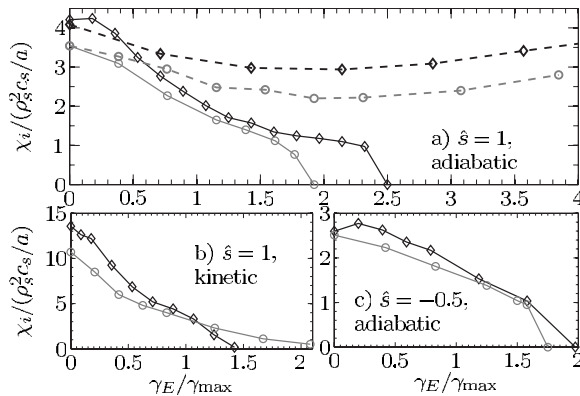


FIG. 4. GWK benchmark of background $\mathbf{E} \times \mathbf{B}$ shear with GYRO. Anomalous ion heat diffusivity against γ_E . GWK results (diamonds) for (a) adiabatic electrons, (b) kinetic electrons, and (c) adiabatic with $\hat{s} = -0.5$ are compared to the equivalent GYRO results (circles) from Tables II, III, IV, and V of Ref. 16. The dashed lines in (a) include coupled parallel velocity shear for purely toroidal rotation with $u_{\parallel}' = 12\gamma_E$.

TABLE II. Representative nonlinear results for $\hat{s}=1$ with mean and variance of saturated quantities.

$\gamma_E(a/c_s)$	$\bar{\chi}_i(a/c_s \rho_s^2)$	$\bar{\Gamma}_{\parallel}/n_i m_i (\rho_s c_s/a)^2$
Adiabatic electrons	$t_{\text{av}} = 1600(a/c_s)$	$t_{\text{av}} = 1600(a/c_s)$
0	4.21 ± 0.65	-0.045 ± 0.297
0.047	3.86 ± 0.42	-0.269 ± 0.257
0.094	2.77 ± 0.24	-0.220 ± 0.149
0.141	2.02 ± 0.16	-0.143 ± 0.095
0.189	1.57 ± 0.12	-0.071 ± 0.060
0.236	1.24 ± 0.08	-0.018 ± 0.043
0.283	1.10 ± 0.09	-0.001 ± 0.032
0.306	0.97 ± 0.14	0.004 ± 0.031
0.330	0	0
Kinetic electrons	$t_{\text{av}} = 255(a/c_s)$	$t_{\text{av}} = 255(a/c_s)$
0.000	13.56 ± 2.95	0.446 ± 0.985
0.047	12.20 ± 3.13	-1.024 ± 0.579
0.094	9.24 ± 1.67	-1.232 ± 0.570
0.141	6.86 ± 1.07	-0.904 ± 0.403
0.189	5.20 ± 0.59	-0.615 ± 0.234
0.236	4.42 ± 0.49	-0.558 ± 0.173
0.283	3.30 ± 0.44	-0.396 ± 0.120
0.330	1.55 ± 0.17	-0.164 ± 0.045
0.377	0	0

For the simulations with adiabatic electrons, there is a sharp transition from the turbulent state at the limit of the critical shear. As was noted in Ref. 16, the region near the critical shear is difficult to resolve properly, indeed this is the region in which the two codes show worst agreement. Simulations conducted with $k_{\perp} \rho_s$ up to 2.05 indicate that the region near the critical shear is sensitive to maximum binormal mode resolution (Fig. 5). This is not surprising since the effect of the shear is to break up structures, pushing the turbulence to smaller scales. While the kinetic case does not exhibit the same sharp transition at high shear, there is still the same difficulty in obtaining a converged result. The higher resolution adiabatic results indicate that the linear quench rule does not well describe the region of $\gamma_E > 1.5\gamma_{\text{max}}$, but further investigation of this is beyond the scope of the present work.

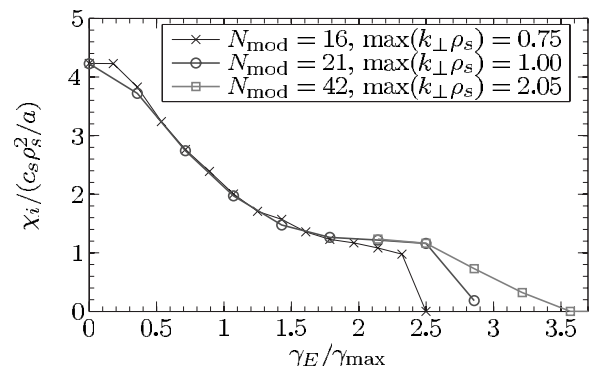
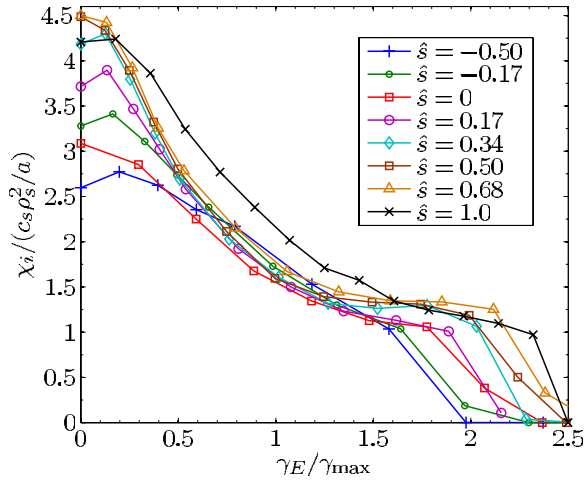


FIG. 5. Comparison of anomalous ion heat diffusivity for the standard and extended binormal resolution with $k_{\perp} \rho_s$ up to 2.05 resolved. The standard resolution is sufficient except in the region near to the critical shear.

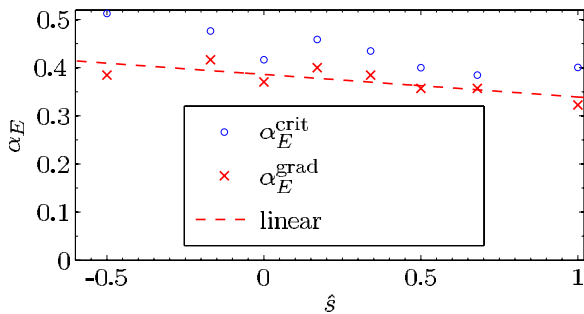
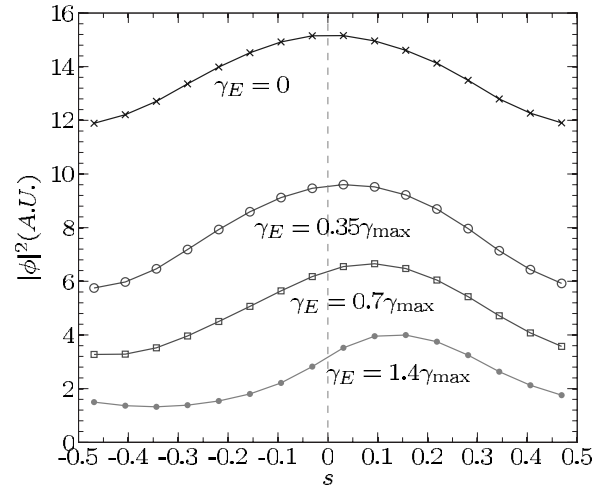
FIG. 6. (Color online) Heat diffusivity against \hat{s} .

A. Parametric dependence of ITG shear quench

For the present work a scan over the magnetic shear is conducted. In Ref. 16 it was noted that the $\hat{s} = -0.5$ case showed a weaker dependence on γ_E than the $\hat{s} = 1$ reference case, and that results for more values of \hat{s} were needed to elucidate this dependence further. GKW results for the ion temperature gradient (ITG) quench rule for various \hat{s} are shown in Fig. 6. The results indicate that for $0.5\gamma_{\max} < \gamma_E < 1.5\gamma_{\max}$ the $\mathbf{E} \times \mathbf{B}$ shear dominates the magnetic shear in regulating the turbulence and there is little variation with \hat{s} . As discussed above, the value of the critical shear for which the turbulence is completely quenched is sensitive to the maximum resolution in the simulation, so values of $(\gamma_E^{\text{crit}} / \gamma_{\max} = 1 / \alpha_E^{\text{crit}})$ should be treated with some caution. We therefore also estimate α_E^{grad} from a line drawn through $\chi_i(\gamma_E = 0)$ and $\chi_i(p)$, where p is the last point before the sharp transition, since Fig. 5 indicates that this point is less affected by the resolution. While we note that this estimate is somewhat arbitrary, within the framework of the established linear quench rule, the values estimated show at least that α_E varies only slowly with \hat{s} (Fig. 7).

IV. PARALLEL MOMENTUM TRANSPORT

The Floquet representation of a single mode eigenfunction in the presence of $\mathbf{E} \times \mathbf{B}$ shear^{40,45} makes clear that the poloidal shift of the ballooning angle⁴⁶ acquires a convection

FIG. 7. (Color online) Variation of shear quench parameter α_E with magnetic shear \hat{s} . Linear fit has equation $\alpha_E^{\text{grad}} = -0.047\hat{s} + 0.39$.FIG. 8. Time averaged perturbed parallel potential showing increasing asymmetry with increasing γ_E . For negative γ_E the direction of the shift is reversed. The case shown has $\hat{s} = 1$. The shift is always in the direction of $s_{\hat{s}} s_B s_j s_j \mathbf{b}$. $s \sim \theta / 2\pi$ is the parallel coordinate.

rate γ_E / \hat{s} . The convected eigenmode will be driven and damped as it passes through the regions of bad and good curvatures, respectively. The $\mathbf{E} \times \mathbf{B}$ shear acts to undo the magnetic twist of structures moving along a field line (Fig. 2 of Ref. 47), with the result that the preferential location for mode growth is shifted away from the outboard midplane, which can be seen when the convected eigenfunction is averaged over $t_{\text{av}} \gg \hat{s} / \gamma_E$.

Clearly this picture (which we call “primary” symmetry breaking) breaks down for small values of $|\hat{s}|$, but gives a qualitative understanding of the physics elsewhere. With this in mind, the use of $s_{\hat{s}} = \pm 1$ in what follows should only be interpreted if $|\hat{s}| > 0.2$. To treat $\mathbf{E} \times \mathbf{B}$ shear for values of \hat{s} close to zero in the ballooning representation requires consideration of higher ballooning mode harmonics (for more details see Ref. 40). In a spectral flux tube code such as GKW, the ballooning formalism is treated spectrally with a shifted periodic toroidal boundary condition³⁷ with the higher ballooning harmonics kept implicitly.

For nonlinear simulations our results show an equilibrium shift in the time average of the parallel solution (Fig. 8) always in the direction of $s_{\hat{s}} s_B s_j s_j \mathbf{b}$. This symmetry breaking is responsible for the $\mathbf{E} \times \mathbf{B}$ contribution to the momentum flux.

A. $\mathbf{E} \times \mathbf{B}$ induced momentum transport: $u'_{\parallel} = 0$

In order to investigate the $\mathbf{E} \times \mathbf{B}$ momentum transport term independently from the diffusive and pinch terms, nonlinear gyrokinetic simulations were performed for the Waltz standard case with $u'_{\parallel} = u_{\parallel} = 0$ with a scan over γ_E and \hat{s} . The $s - \alpha$ equilibrium model used has up-down symmetric flux surfaces, so for these simulations all terms in Eq. (2) are zero except for the $M_{\parallel} \gamma_E$ term due to $\mathbf{E} \times \mathbf{B}$ shear. Since these simulations produce nonzero values for the parallel momentum flux Γ_{\parallel} , the system is not in the null flow state of equilibrium rotation.

TABLE III. Representative nonlinear results for $\gamma_E=0.141(c_s/a)$ with mean and variance of time averaged saturated quantities.

\hat{s}	$\bar{\chi}_i(a/c_s\rho_s^2)$	$\bar{\Gamma}_i(a/c_s\rho_s^2)$
Adiabatic electrons		
-0.50	1.53 ± 0.10	-0.143 ± 0.095
-0.17	1.73 ± 0.11	-0.193 ± 0.109
0.00	1.68 ± 0.13	-0.181 ± 0.107
0.17	1.92 ± 0.15	-0.166 ± 0.088
0.34	2.03 ± 0.20	-0.096 ± 0.074
0.50	2.11 ± 0.18	-0.066 ± 0.055
0.68	2.15 ± 0.18	0.046 ± 0.056
1.00	2.02 ± 0.16	0.124 ± 0.046

Since the results presented form a two dimensional parameter scan, we list only selected representative results in tabular form; Table II shows the variation of fluxes with γ_E for $\hat{s}=1$, and Table III shows the variation of the fluxes against \hat{s} for $\gamma_E=0.141(c_s/a)$.

The results for momentum flux are shown in Fig. 9. As expected, the $\mathbf{E} \times \mathbf{B}$ contribution exhibits a maximum in the shearing rate, but it can also be seen that the results exhibit a nonlinear dependence on the magnetic shear. To examine this further, we deconstruct the results by examining ratio quantities of interest.

Since the turbulence follows a linear quench rule [Eq. (5)], the quantity $\Gamma_{||}/\chi_i$ plotted in Fig. 10 represents the strength of the symmetry breaking $\mathbf{E} \times \mathbf{B}$ contribution with the background level of the turbulence (quantified by χ_i) factored out. These results show that the cases with $0 < \hat{s} < 0.5$ behave differently to the outlying values of the magnetic shear, since the ratio $\Gamma_{||}/\chi_i$ grows with γ_E . We conclude that the behavior of the $\mathbf{E} \times \mathbf{B}$ momentum contribution to transport strongly depends on the magnetic shear. The results also clearly show that “secondary” symmetry breaking still occurs for the $\hat{s}=0$ case, the mechanism of which is not covered by the Floquet mode picture described above. This case could be treated with a purely periodic formalism not requiring the ballooning transform, where further analytic work could elucidate the secondary symmetry breaking mechanism.

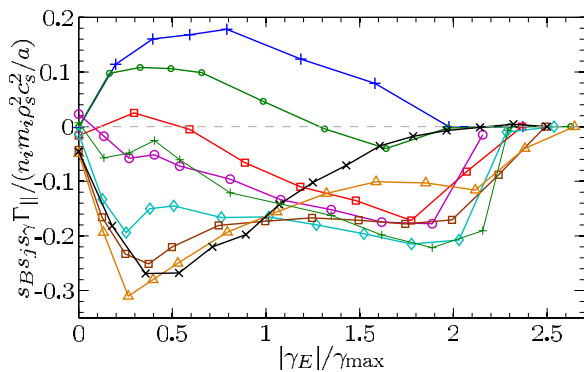
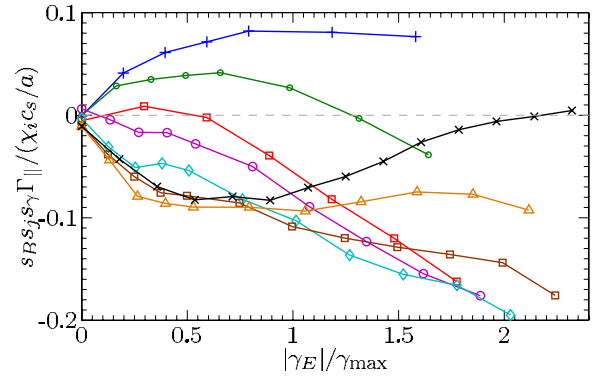
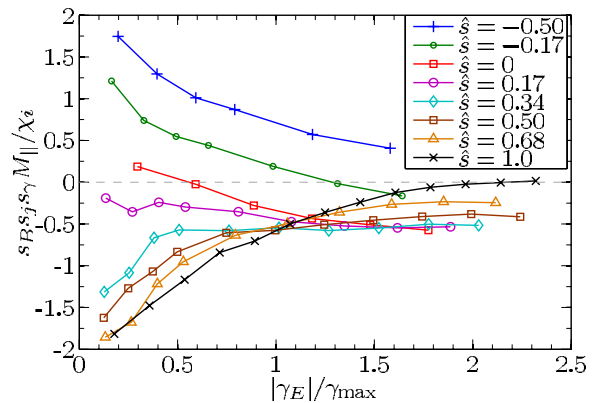
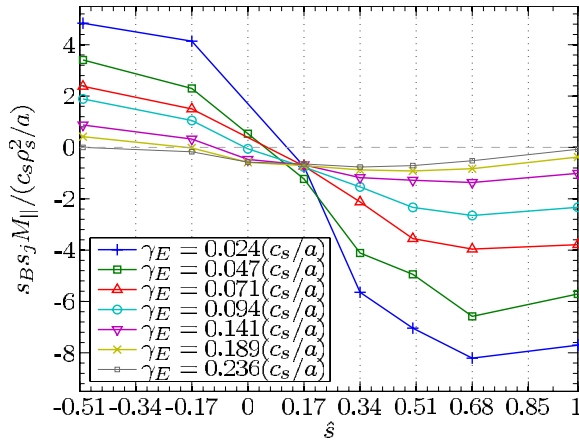
FIG. 9. (Color online) Momentum transport due to $\mathbf{E} \times \mathbf{B}$ shear contribution for different values of \hat{s} . Legend as for Figs. 1, 6, and 11.FIG. 10. (Color online) Momentum transport due to $\mathbf{E} \times \mathbf{B}$ shear contribution normalized with heat diffusivity for different values of \hat{s} . Legend as for Figs. 1, 6, and 11.

Figure 11 plots the dimensionless quantity $M_{||}/\chi_i$; the momentum transport due to $\mathbf{E} \times \mathbf{B}$ shear with the assumed dependence on both the level of the turbulence and the rate of the shearing factored out. The conclusion drawn from Fig. 11 is that even after factoring out the quenching of turbulence, the dependence on γ_E of the $\mathbf{E} \times \mathbf{B}$ contribution to momentum transport is stronger than linear. This demonstrates the limitation of the heuristic linear model [Eq. (2)]. For $0 < \hat{s} < 0.5$, the value of $M_{||}/\chi_i$ saturates at around -0.5 beyond $\gamma_E/\gamma_{\max} \approx 1$.

Slicing orthogonally through the (\hat{s}, γ_E) parameter space, we see that $M_{||}$ is not exactly symmetric about $\hat{s}=0$ (Fig. 12), i.e., that the secondary symmetry breaking mechanism is present at all values of \hat{s} , although in most cases is dominated by the primary Floquet mechanism. The result is that $\hat{s}=0.17$ is a stationary point where $M_{||}$ is constant over a range of γ_E .

The sign of the $\mathbf{E} \times \mathbf{B}$ contribution to the momentum flux reverses with each of s_B , s_j , and s_γ . We emphasize that in this work the definition of $u_{||}$ is positive in the direction of \mathbf{B} , and that positive $\Gamma_{||}$ is transport of cofield rotation radially outwards. In the laboratory frame, then, flipping the toroidal field does not alter the direction of the rotation resulting from the $\mathbf{E} \times \mathbf{B}$ contribution to momentum transport. If ∇E_r is radially outwards and $\hat{s} > 0.2$ the effect of the $\mathbf{E} \times \mathbf{B}$ momentum flux is to spin up the core counter to the plasma current.

FIG. 11. (Color online) Momentum fluxes normalized with heat diffusivity and γ_E for different values of \hat{s} .

FIG. 12. (Color online) $M_{||}$ against \hat{s} for various γ_E .

B. Coupling to momentum diffusivity: $u'_{||} \neq 0$

The terms in the heuristic breakdown of anomalous momentum transport [Eq. (2)] all depend on the background level of turbulence [Eq. (5)]. These contributions to parallel momentum transport cannot be considered independent since parallel velocity shear both drives turbulence (anti-quench) and causes diffusive transport, while γ_E both quenches turbulence and drives nondiffusive momentum transport. This dependence on the background turbulence can be factored out, (as in the previous section) by normalizing each term with the ion heat diffusivity χ_i to give dimensionless ratios. In the linear models,^{18,27} it is implicitly assumed that these dimensionless quantities are slowly varying over parameter space. Here, we examine this assumption for both the diffusive term and the $\mathbf{E} \times \mathbf{B}$ contribution to the momentum transport [first and third terms in Eq. (2)]. Additional adiabatic simulations were performed over $(u'_{||}, \gamma_E)$ parameter space by holding a nonzero value of γ_E constant for a range of $u'_{||}$ (This is distinct from the case of toroidal coupling, which is discussed in Sec. IV C.). The resulting momentum fluxes therefore contain both the diffusive and $\mathbf{E} \times \mathbf{B}$ contributions to the momentum transport from which the assumed dimensionless constants can be calculated. The simulations in this section were performed with $N_{\text{mod}}=21$ and $k_{\perp} \rho_s$ up to 1.00.

The normalized diffusive term (Prandtl number) in the heuristic model can be estimated from

$$P_R(u'_{||}, \gamma_E) = \frac{\chi_{||}^{\text{est}}}{\chi_i} = \frac{\Gamma_{||}(u'_{||}, \gamma_E) - \Gamma_{||}(0, \gamma_E)}{u'_{||} \chi_i(u'_{||}, \gamma_E)}, \quad (7)$$

the calculated values for which are plotted in Fig. 13 (middle), indicating that the Prandtl number is roughly constant over a range of both $u'_{||}$ and γ_E .

The normalized contribution of the $\mathbf{E} \times \mathbf{B}$ term alone (also dimensionless) in the heuristic model can be estimated from

$$M_R(u'_{||}, \gamma_E) = \frac{M_{||}^{\text{est}}}{\chi_i} = \frac{\Gamma_{||}(u'_{||}, \gamma_E) - \Gamma_{||}(u'_{||}, 0)}{\gamma_E \chi_i(u'_{||}, \gamma_E)}, \quad (8)$$

the calculated values for which are plotted in Fig. 13 (lower). The figure shows that for $\gamma_E \ll \gamma_{\text{max}}$ the $\mathbf{E} \times \mathbf{B}$ contribution can be argued to be constant, but this is not the case for

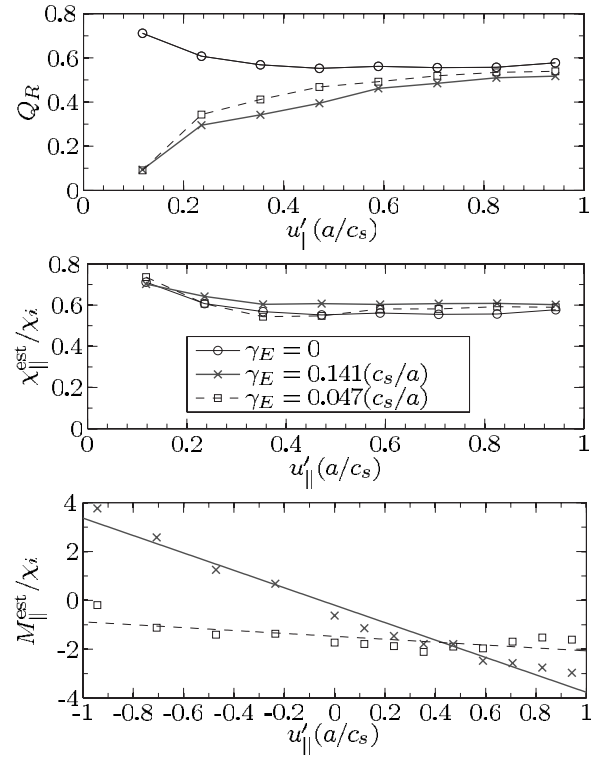


FIG. 13. Q_R (upper) converges to the estimated Prandtl number $P_R^{\text{est}}=0.6$ (middle). The curve for $\gamma_E=0$ (circles) is the same in the top two figures. M_R (lower) is only independent of $u'_{||}$ for small values of γ_E . The legend is the same for all three figures. The linear fits used in the bottom figure are $M_R = (-0.60, -3.57)u'_{||}(a/c_s) - (1.47, 0.20)$ (dashed, solid).

larger $\gamma_E \sim \gamma_{\text{max}}$, with the inclusion of parallel flow shear amplifying the $\mathbf{E} \times \mathbf{B}$ contribution to the momentum transport. For negative $u'_{||}$, the sign of $M_{||}$ is even found to invert. In the previous section it was demonstrated that the $\mathbf{E} \times \mathbf{B}$ contribution was quenched by γ_E more strongly than the heat flux quench rule; here we see the converse. The turbulence is driven by the destabilizing parallel flow shear, and the $\mathbf{E} \times \mathbf{B}$ contribution is amplified. These two results both demonstrate that the $\mathbf{E} \times \mathbf{B}$ contribution has a stronger than linear dependence on the background level of turbulence, which is not captured by the heuristic breakdown.

We also define the dimensionless number

$$Q_R = \frac{\Gamma_{||}/u'_{||}}{\chi_i} = \chi_{||}^{\text{eff}}/\chi_i, \quad (9)$$

which is distinct from the Prandtl number since the momentum transport in this case is not purely diffusive. The value of Q_R is plotted in Fig. 13 (upper).

Despite the amplification of $M_{||}$ with $u'_{||}$, the value of Q_R converges with $u'_{||}$ to close to the Prandtl number $P_R \approx 0.6$ irrespective of γ_E ($<7\%$ difference) [Fig. 13 (upper)], since the diffusive term still dominates the slower variation of $M_{||}$ with $u'_{||}$.

Keeping only the rotational terms (diffusive, $\mathbf{E} \times \mathbf{B}$, and Coriolis) of Eq. (2) without the toroidal rotation linking of $u'_{||}$ and γ_E , locating null flow points ($\Gamma_{||}=0$) requires expensive scans over $(u_{||}, u'_{||}, \gamma_E)$ parameter space. Using the

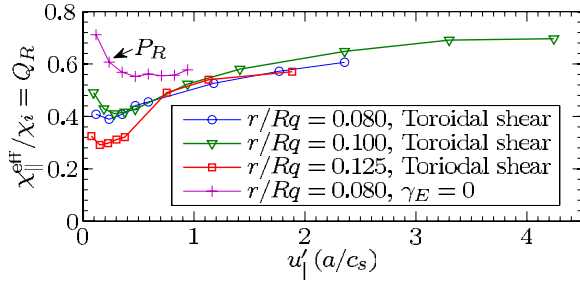


FIG. 14. (Color online) Effective momentum diffusivity χ_{eff} for cases with purely toroidal rotation [$u'_{\parallel} = (Rq/r)\gamma_E$]. The aspect ratio r/R was varied between 0.16, 0.20, and 0.25, with the safety factor $q=2$ unchanged.

assumption of independence of the terms in Eq. (2), valid for $\gamma_E \ll \gamma_{\text{max}}$, we estimate the location of null flow points for $u=0$.

Using the value $P_R=0.6$ for the Prandtl number determined above, and the results for M_{\parallel}/χ_i shown in Fig. 11, we estimate that for the $\hat{s}=1$ case there is one example of a null flow point at $(u'_{\parallel}, \gamma_E) \approx (0.1, 0.04)(c_s/a)$, but none for $u'_{\parallel} > 0.14(c_s/a)$. In Ref. 22, slightly different null flow points were found for $u'_{\parallel}=0.1, 0.2$ but not for $u'_{\parallel}=0.3$ or greater. For the case with $\hat{s}=0.5$ we again find the Prandtl number $P_R \approx 0.6$ and a similar null flow point at $(u'_{\parallel}, \gamma_E) \approx (0.1, 0.05)(c_s/a)$. Since the curve of $\Gamma_{\parallel}/\chi_i$ (Fig. 10) for $\hat{s}=0.5$ does not turn over there may also exist null flow points at greater values of γ_E , but these cannot be estimated accurately since (as discussed above) M_{\parallel} is enhanced for $\gamma_E \sim \gamma_{\text{max}}$ with $u'_{\parallel} > 0$. We stress that the existence of null flow points requires $s_{\hat{s}}s_{\gamma}s_{j}s_B=1$ since the sign of the $\mathbf{E} \times \mathbf{B}$ momentum flux inverts with each of the sign coefficients.

C. Sheared toroidal rotation

For the case of purely toroidal rotation, the parallel and perpendicular flows are coupled such that the poloidal components cancel, with $u'_{\parallel} = s_B s_j (R|q|/r)\gamma_E$ in the $s-\alpha$ geometry model with $u_{\parallel}=0$. While $\mathbf{E} \times \mathbf{B}$ shear quenches transport, parallel velocity shear is destabilizing. With the coupling of the parallel velocity shear drive, the turbulence can be sustained in the limit of large γ_E . An effective momentum diffusivity can be defined including the $\mathbf{E} \times \mathbf{B}$ momentum transport as a correction

$$\chi_{\parallel}^{\text{eff}} = \chi_{\parallel} + s_B s_j \frac{r}{R|q|} M_{\parallel}. \quad (10)$$

For magnetic shear $\hat{s} > 0.17$, the $\mathbf{E} \times \mathbf{B}$ shear contribution to momentum transport has $\text{sign}(M_{\parallel}) = -s_B s_j$ (Fig. 11) and always acts to reduce the effective diffusivity irrespective of the direction of plasma current and toroidal field. Equivalently, the $\mathbf{E} \times \mathbf{B}$ contribution for $\hat{s} > 0.17$ always transports clockwise momentum in the direction of ∇E_r , which is determined by the direction of any existing peaked rotation profile.

To examine the case of toroidal rotation, further simulations were conducted including both the parallel shear u'_{\parallel} and the perpendicular shear γ_E coupled for purely toroidal rotation. Since the size of correction is partly determined by

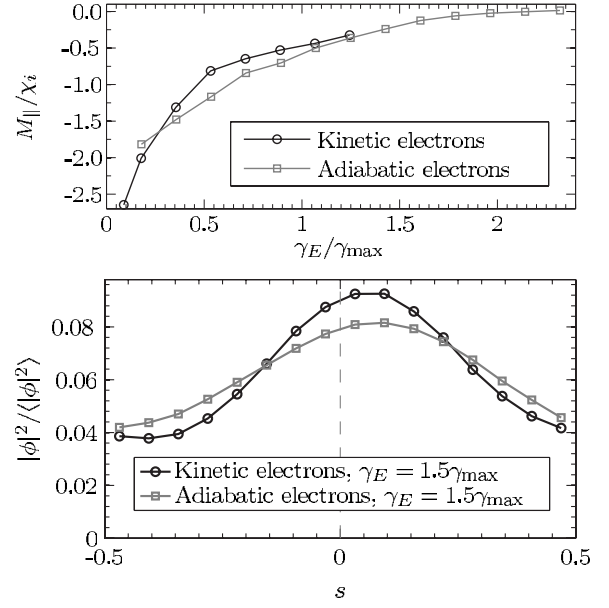


FIG. 15. (Top) Comparison of normalized M_{\parallel} for kinetic electrons and adiabatic electrons. (Bottom) Parallel perturbed potential structures compared. The trapped electron drive is localized on the outboard side, but the asymmetric shift is equivalent.

geometry parameters, the aspect ratio $\epsilon = r/R$ was varied between 0.16, 0.20, and 0.25, and scans were conducted over u'_{\parallel} . The safety factor $q=2$ was held constant. For the values of ϵ used (and for the other specific parameters of this case), the diffusive correction can be up to 50% (Fig. 14). It is possible that for other cases (e.g., lower q or larger ϵ) the correction could dominate, resulting in null flow or a negative effective diffusivity. The convergence of Q_R in Fig. 14 occurs slower than in Fig. 13 (upper) because in the toroidal shear case γ_E increases in tandem with u'_{\parallel} , increasing the $\mathbf{E} \times \mathbf{B}$ correction to the momentum transport.

D. Kinetic electrons

Finally, we examine the effect of trapped electrons on the $\mathbf{E} \times \mathbf{B}$ momentum transport. In Fig. 15 (Top) the momentum fluxes for $(u'_{\parallel}, \hat{s}) = (0, 1)$ are shown to be comparable with the adiabatic case once the increased turbulence due to the trapped electron drive is factored out. Comparing the parallel potential structure Fig. 15 (Bottom), we see an equivalent asymmetric shift for the kinetic and adiabatic cases. This differs from the Coriolis pinch¹⁸ in which the Coriolis drift generates an asymmetry in the parallel velocity structure, and the potential shift in response compensates (completely in the case of adiabatic electrons) the symmetry breaking of the Coriolis drift.¹⁹ Here, no such “compensation effect” occurs since the asymmetry in the solution is generated directly through the convection and effective shift of the ballooning angle.

V. DISCUSSION AND CONCLUSIONS

Nonlinear local gyrokinetic simulations have confirmed the quasilinear slab prediction of parallel momentum transport due to the background $\mathbf{E} \times \mathbf{B}$ shear,¹² generated by sym-

metry breaking. The sheared $\mathbf{E} \times \mathbf{B}$ flow both quenches turbulence while driving a parallel asymmetry that produces anomalous parallel momentum transport. Given these competing effects, the turbulent momentum transport due to this term in isolation exhibits an extrema in the shearing rate γ_E (as predicted in Ref. 12).

The simulations show that the $\mathbf{E} \times \mathbf{B}$ contribution to the momentum transport ($M_{\parallel} \gamma_E$) has a stronger dependence on γ_E than that observed for the heat diffusivity, such that the dimensionless number $M_R = M_{\parallel} / \chi_i$ is not constant. The simulations also demonstrate that the behavior of M_R relative to the background turbulence strongly depends on the magnetic shear \hat{s} , and also depends on the parallel and perpendicular velocity gradients. It is likely that M_{\parallel} will also vary with toroidal flow u_{\parallel} , but this is not studied in the present work.

The direction of the $\mathbf{E} \times \mathbf{B}$ induced momentum transport depends on the plasma current direction and also reverses with the sign of ∇E_r and \hat{s} , such that for ∇E_r radially outwards and positive magnetic shear, the tendency is to spin up the plasma core counter to the plasma current. We also find that secondary $\mathbf{E} \times \mathbf{B}$ symmetry breaking generates momentum transport at zero magnetic shear.

For low parallel flow gradients, the size of the $\mathbf{E} \times \mathbf{B}$ contribution can be a significant correction to the diffusive momentum transport, under certain conditions resulting in null flow sustaining equilibrium rotation gradients. For positive magnetic shear, the effect is to enhance any existing rotation gradient responsible for a radial electric field gradient ∇E_r . While the Coriolis pinch¹⁸ requires a seed rotation, for this effect a gradient in the initial rotation must be present. In the case of purely toroidal rotation, the effective momentum diffusivity can be significantly reduced at lower toroidal rotation gradients.

Since the sign of $\mathbf{E} \times \mathbf{B}$ contribution to momentum transport reverses with the magnetic shear, parallel momentum can be transported toward a minimum in the q -profile if $s_{FS} s_{\gamma} = 1$. This local “spin up” may play a role in the formation of some ITBs, especially if (as indicated in Ref. 7) the poloidal flows in the region of a transport barrier are elevated well above the neoclassical level. A fully consistent treatment of barrier formation and rotation will require consistent calculation of neoclassical poloidal flows and turbulent poloidal momentum transport.^{12,48}

Simulations including trapped electron drive demonstrated comparable results to those with adiabatic electrons, with no compensation effect (as seen for the Coriolis pinch¹⁹) observed. The case examined was ITG mode dominated and a trapped electron mode case could produce different behavior.

In summary, while the diffusive parallel momentum Prandtl number is roughly constant over a range of parameter space, this work shows that the equivalent dimensionless ratio for $\mathbf{E} \times \mathbf{B}$ induced momentum transport is a strong function of shearing rate, parallel flow gradient, and magnetic shear.

ACKNOWLEDGMENTS

The authors would like to thank G. Hammett, W. Dorland, and W. Guttenfelder for useful discussions. This work was funded by EPSRC in association with UKAEA Culham and simulations were performed using the resources of the Centre for Scientific Computing at the University of Warwick.

- ¹J. Rice, M. Greenwald, I. Hutchinson, E. Marmar, Y. Takase, S. Wolfe, and F. Bombarda, *Nucl. Fusion* **38**, 75 (1998).
- ²I. H. Hutchinson, J. E. Rice, R. S. Granetz, and J. A. Snipes, *Phys. Rev. Lett.* **84**, 3330 (2000).
- ³J. Rice, W. Lee, E. Marmar, P. Bonoli, R. Granetz, M. Greenwald, A. Hubbard, I. Hutchinson, J. Irby, Y. Lin, D. Mossessian, J. A. Snipes, S. M. Wolfe, and S. J. Wukitch, *Nucl. Fusion* **44**, 379 (2004).
- ⁴A. Bortolon, B. P. Duval, A. Pochelon, and A. Scarabosio, *Phys. Rev. Lett.* **97**, 235003 (2006).
- ⁵J. S. deGrassie, J. E. Rice, K. H. Burrell, R. J. Groebner, and W. M. Solomon, *Phys. Plasmas* **14**, 056115 (2007).
- ⁶J. Rice, A. Ince-Cushman, J. deGrassie, L.-G. Eriksson, Y. Sakamoto, A. Scarabosio, A. Bortolon, K. Burrell, B. Duval, C. Fenzi-Bonizec, M. J. Greenwald, R. J. Groebner, G. T. Hoang, Y. Koide, E. S. Marmar, A. Pochelon, and Y. Podpaly, *Nucl. Fusion* **47**, 1618 (2007).
- ⁷T. Tala, Y. Andrew, K. Crombe, P. de Vries, X. Garbet, N. Hawkes, H. Nordman, K. Rantamaki, P. Strand, A. Thyagaraja, J. Weiland, E. Asp, Y. Baranov, C. Challis, G. Corrigan, A. Eriksson, C. Giroud, M.-D. Hua, I. Jenkins, H. C. M. Knoop, X. Litaudon, P. Mantica, V. Naulin, V. Parail, and K.-D. Zastrow, *Nucl. Fusion* **47**, 1012 (2007).
- ⁸W. M. Solomon, K. H. Burrell, J. S. deGrassie, R. Budny, R. J. Groebner, J. E. Kinsey, G. J. Kramer, T. C. Luce, M. A. Makowski, D. Mikkelsen, R. Nazikian, C. C. Petty, P. A. Politzer, S. D. Scott, M. A. Van Zeeland, and M. C. Zarnstorff, *Plasma Phys. Controlled Fusion* **49**, B313 (2007).
- ⁹T. Tala, K.-D. Zastrow, J. Ferreira, P. Mantica, V. Naulin, A. G. Peeters, G. Tardini, M. Brix, G. Corrigan, C. Giroud, and D. Strintzi, *Phys. Rev. Lett.* **102**, 075001 (2009).
- ¹⁰S. Kaye, W. Solomon, R. Bell, B. LeBlanc, F. Levinton, J. Menard, G. Rewoldt, S. Sabbagh, W. Wang, and H. Yuh, *Nucl. Fusion* **49**, 045010 (2009).
- ¹¹G. Tardini, J. Ferreira, P. Mantica, A. G. Peeters, T. Tala, K. D. Zastrow, M. Brix, C. Giroud, and G. V. Pereverzev, *Nucl. Fusion* **49**, 085010 (2009).
- ¹²R. R. Dominguez and G. M. Staebler, *Phys. Fluids B* **5**, 3876 (1993).
- ¹³X. Garbet, Y. Sarazin, P. Ghendrih, S. Benkadda, P. Beyer, C. Figarella, and I. Voitsekhovitch, *Phys. Plasmas* **9**, 3893 (2002).
- ¹⁴A. G. Peeters and D. Strintzi, *Phys. Plasmas* **11**, 3748 (2004).
- ¹⁵A. G. Peeters and C. Angioni, *Phys. Plasmas* **12**, 072515 (2005).
- ¹⁶J. E. Kinsey, R. E. Waltz, and J. Candy, *Phys. Plasmas* **12**, 062302 (2005).
- ¹⁷A. G. Peeters, C. Angioni, A. Bottino, A. Kallenbach, B. Kurzan, C. F. Maggi, and W. Suttrop, *Plasma Phys. Controlled Fusion* **48**, B413 (2006).
- ¹⁸A. G. Peeters, C. Angioni, and D. Strintzi, *Phys. Rev. Lett.* **98**, 265003 (2007).
- ¹⁹A. G. Peeters, C. Angioni, Y. Camenen, F. J. Casson, W. A. Hornsby, A. P. Snodin, and D. Strintzi, *Phys. Plasmas* **16**, 062311 (2009).
- ²⁰Y. Camenen, A. G. Peeters, C. Angioni, F. J. Casson, W. A. Hornsby, A. P. Snodin, and D. Strintzi, *Phys. Plasmas* **16**, 012503 (2009).
- ²¹A. G. Peeters, D. Strintzi, Y. Camenen, C. Angioni, F. J. Casson, W. A. Hornsby, and A. P. Snodin, *Phys. Plasmas* **16**, 042310 (2009).
- ²²R. E. Waltz, G. M. Staebler, J. Candy, and F. L. Hinton, *Phys. Plasmas* **14**, 122507 (2007).
- ²³O. D. Gürcan, P. H. Diamond, T. S. Hahm, and R. Singh, *Phys. Plasmas* **14**, 042306 (2007).
- ²⁴O. D. Gürcan, P. H. Diamond, and T. S. Hahm, *Phys. Rev. Lett.* **100**, 135001 (2008).
- ²⁵P. H. Diamond, C. J. McDevitt, O. D. Gürcan, T. S. Hahm, and V. Naulin, *Phys. Plasmas* **15**, 012303 (2008).
- ²⁶D. Strintzi, A. G. Peeters, and J. Weiland, *Phys. Plasmas* **15**, 044502 (2008).
- ²⁷Y. Camenen, A. G. Peeters, C. Angioni, F. J. Casson, W. A. Hornsby, A. P. Snodin, and D. Strintzi, *Phys. Rev. Lett.* **102**, 125001 (2009).
- ²⁸Y. Camenen, A. G. Peeters, C. Angioni, F. J. Casson, W. A. Hornsby, A. P. Snodin, and D. Strintzi, *Phys. Plasmas* **16**, 062501 (2009).
- ²⁹T. S. Hahm, P. H. Diamond, O. D. Gürcan, and G. Rewoldt, *Phys. Plasmas*

- 15**, 055902 (2008).
- ³⁰A. G. Peeters, C. Angioni, and D. Strintzi, *Phys. Plasmas* **16**, 034703 (2009).
- ³¹I. Holod and Z. Lin, *Phys. Plasmas* **15**, 092302 (2008).
- ³²W. X. Wang, T. S. Hahm, S. Ethier, G. Rewoldt, W. W. Lee, W. M. Tang, S. M. Kaye, and P. H. Diamond, *Phys. Rev. Lett.* **102**, 035005 (2009).
- ³³H. Biglari, P. H. Diamond, and P. W. Terry, *Phys. Fluids B* **2**, 1 (1990).
- ³⁴R. E. Waltz, G. D. Kerbel, and J. Milovich, *Phys. Plasmas* **1**, 2229 (1994).
- ³⁵R. C. Wolf, *Plasma Phys. Controlled Fusion* **45**, R1 (2003).
- ³⁶J. Connor, T. Fukuda, X. Garbet, C. Gormezano, V. Mukhovatov, and M. Wakatani, *Nucl. Fusion* **44**, R1 (2004).
- ³⁷A. G. Peeters, Y. Camenen, F. J. Casson, W. A. Hornsby, A. P. Snodin, D. Strintzi, and G. Szepesi, "The nonlinear gyro-kinetic flux tube code GKW," *Comput. Phys. Commun.* (in press) .
- ³⁸R. E. Waltz, G. D. Kerbel, J. Milovich, and G. W. Hammett, *Phys. Plasmas* **2**, 2408 (1995).
- ³⁹R. E. Waltz, G. M. Staebler, W. Dorland, G. W. Hammett, M. Kotschenreuther, and J. A. Konings, *Phys. Plasmas* **4**, 2482 (1997).
- ⁴⁰R. E. Waltz, R. L. Dewar, and X. Garbet, *Phys. Plasmas* **5**, 1784 (1998).
- ⁴¹R. E. Waltz, J. M. Candy, and M. N. Rosenbluth, *Phys. Plasmas* **9**, 1938 (2002).
- ⁴²T. S. Hahm and K. H. Burrell, *Phys. Plasmas* **2**, 1648 (1995).
- ⁴³K. H. Burrell, *Phys. Plasmas* **4**, 1499 (1997).
- ⁴⁴G. W. Hammett, W. Dorland, N. F. Loureiro, and T. Tatsuno, *Bull. Am. Phys. Soc.* **VP1**, 136 (2006).
- ⁴⁵J. W. Connor, J. B. Taylor, and H. R. Wilson, *Phys. Rev. Lett.* **70**, 1803 (1993).
- ⁴⁶J. W. Connor, R. J. Hastie, and J. B. Taylor (UKAEA Culham), *Phys. Rev. Lett.* **40**, 396 (1978).
- ⁴⁷J. T. M. Antonsen, J. F. Drake, P. N. Guzdar, A. B. Hassam, Y. T. Lau, C. S. Liu, and S. V. Novakovskii, *Phys. Plasmas* **3**, 2221 (1996).
- ⁴⁸P. H. Diamond and Y.-B. Kim, *Phys. Fluids B* **3**, 1626 (1991).